journal of the mechanical behavior of biomedical materials 155 (2024) 106541

Contents lists available at ScienceDirect

Journal of the Mechanical Behavior of Biomedical Materials

journal homepage: www.elsevier.com/locate/jmbbm

Approach for contact medical device development via integrated testing, skeletal muscle modeling, and finite element analysis

Conor Shanley [a], Q. Jane Wang [a,*], Bruce Livingston [b]

[a] Mechanical Engineering, Northwestern University, Evanston, IL, 60208, USA
[b] MedWitness, Skokie, IL, 60076, USA

A B S T R A C T

Development of novel medical devices for the treatment of musculoskeletal pain associated with neuro-muscular trigger points requires a model for relating the mechanical responses of *in vivo* biological tissues to applied palliative physical pressures and a method to design treatments for optimal effects. It is reasonable to hypothesize that the efficacy of therapeutic treatment is proportional to the maximum tensile strain at trigger point locations. This work presents modeling of the mechanical behavior of biological tissue structures and treatment simulations, supported by indentation experiments and finite element (FE) modeling. The steady-state indentation responses of the tissue structure of the posterior neck were measured with a testing device, and an FE model was constructed using a first-order Ogden hyperelastic material model and calibrated with the experimental data. The error between experimental and FE-generated displacement-load curves was minimized via a two-stage optimization process comprised of an Optimal Latin Hypercube design-of-experiments analysis and a Bayesian optimization loop. The optimized Ogden model had an initial shear modulus (μ) of 5.16 kPa and a deviatoric exponent (α) of 11.90. Another FE model was developed to simulate the deformation of the tissue structures in the posterior neck adjacent to the C3 vertebrae in response to indentation loading, in order to determine the optimal location and angle to apply an indentation force for maximum therapeutic benefit. The optimal location of indentation was determined to be 28° lateral from the sagittal plane along the surface of the skin, measured from the centerline of the spine, at an angle of 8° counterclockwise from the surface normal vector. The optimized spatial orientation of the indentation corresponded to the average of the maximum principal strain across the deep muscle region of the model.

1. Introduction

Myofascial pain syndrome (MPS) is a common musculoskeletal disorder that affects a large percentage of the world population and is characterized by focal spots in skeletal muscle which are the source of local and referred pain, also known as trigger points (Alvarez and Rockwell, 2002; Yap, 2007). Trigger points may also cause a reduced range of motion for the affected muscle(s). While there is insufficient evidence to identify a universal cause for myofascial pain, research suggests that poor posture, nervous tension, biochemical abnormalities, electrolyte imbalances, and activities that cause repetitive stresses to particular muscles or muscle groups (Alvarez and Rockwell, 2002; Yap, 2007; Simons et al., 1999; Niel-Asher, 2014) may contribute to its development. In addition, MPS specifically in the head and neck region may also cause tinnitus, headaches, and jaw issues (Alvarez and Rockwell, 2002). The excitation of trigger points by physical means or the interference of trigger point neural circuitry by pharmaceutical means are known effective methods of treating MPS (Simons et al., 1999; Grieve et al., 2011; Montanez-Aguilera et al., 2010; Wiaderna et al., 2022). Excitation of trigger points achieves a dampening effect on the pain by fatiguing the nervous system circuit to and from the trigger point, resulting in a loss of signal intensity. Pharmacological agents, on the other hand, achieve the same pain-dampening effect by blocking the nerve signals directly. With both approaches, there is a time lag between the application of the therapy and loss of signal(s). The pharmacological agents need time to be absorbed into the system and accumulate at the site where they work to block the signal directly, either at the local level or in the spine and brain. The excitation approach takes time to cause the local circuits to deplete the necessary chemicals which carry the electro-chemical current that transmits the pain signal.

Trigger points are characterized by small clusters of muscle fibers in spasm, approximately 2–10 mm in size, located in the body of a muscle (Niel-Asher, 2014). Trigger points may be treated in several ways. Pharmaceutical treatments include muscle relaxants, pain relievers (analgesics) and anti-inflammatory medications (Ickowicz et al., 2009), whereas non-pharmaceutical remedies include acupuncture, acupressure, massage, and temperature treatments, among others (Grieve et al., 2011; Montanez-Aguilera et al., 2010; Wiaderna et al., 2022; Delgado et al., 2010). While many treatments aim to mitigate pain by reducing inflammation, exciting chemicals that block sensory nerve conduction,

* Corresponding author.
E-mail address: qwang@northwestern.edu (Q.J. Wang).

https://doi.org/10.1016/j.jmbbm.2024.106541
Received 3 February 2024; Received in revised form 1 April 2024; Accepted 9 April 2024
Available online 16 April 2024

and promoting blood flow to the affected area, applying manual pressure to stretch the muscle fibers in spasm in the trigger point is particularly effective (Grieve et al., 2011; Montanez-Aguilera et al., 2010; Wiaderna et al., 2022). The Fascial Distortion Model (FDM) prescribes specific techniques of deep-tissue acupressure intervention, shown to reduce pain intensity and improve the range of motion of the affected muscle groups (Wiaderna et al., 2022). Such treatment also removes exposure of the patient to the side effects of chronic drug use.

In general, skeletal muscle contains special sets of intrafusal muscle fibers known as muscle spindles, which communicate with the spinal cord via motor and sensory neurons, facilitating feedback to the central nervous system (CNS) related to the state of muscle stretch (Levangie et al., 2019). Muscles can enter a state of prolonged contraction, commonly referred to as muscle spasm. Spasms must be interrupted and the muscles allowed to return to their normal state of equilibrium and neutral anatomic position to eliminate pain and restore the full range of motion (Levangie et al., 2019; Mukherjee and Chakravarty, 2010).

The application of physical pressure to a trigger point has been shown to be an effective means of treatment (Grieve et al., 2011; Montanez-Aguilera et al., 2010; Wiaderna et al., 2022). Pressure can help alleviate pain and heal the tissue in spasm by way of several mechanisms. Firstly, stretching muscle fibers that are in spasm physically opposes the contractile motion of the muscles, and instead forces the muscles to elongate. It is important to note that the object of stretching should not be to present an equal and opposite force to elongate the fibers in spasm, as this may have an adverse effect and increase the overall muscle trauma (Adams et al., 2010). Instead, it is beneficial to apply a lower magnitude stretching force gradually, so as to promote muscle relaxation by fatiguing the muscle without greatly increasing immediate muscle strain. The FDM techniques, for example, often apply manual palpitation over a period of 10–20 s, until muscle relaxation is detected by the administering therapist (Wiaderna et al., 2022).

Application of physical pressure has additional beneficial effects to treat both the root cause and symptoms of trigger points. Generally, muscles in spasm generate lactic acid as a byproduct of the partial anaerobic metabolic processes of the muscle cells, which is a caustic chemical that penetrates into the surrounding connective tissue and causes pain, irritation, and soreness in the affected tissue (Gladden, 2008). Pressure application can forcibly remove lactic acid from the affected tissue, allowing it to be leached away by absorption into the venous and lymphatic vessels, alleviating pain and soreness (Adamczyk et al., 2020). Distortion of the tissue created by physical pressure increases arterial blood flow to the affected area, aiding in the recovery process by delivering oxygen, water, proteins, and other nutrients to the area (Adamczyk et al., 2020). Finally, palpitation of the affected tissue can over-excite the muscle spindle, causing the nerves to fatigue and cease to transmit pain signals (Campbell et al., 2020; Astokorki and Mauger, 2017). In summation, the treatment of trigger points through application of physical pressure offers multiple simultaneous therapeutic benefits.

Professionally administered physical therapy treatments remain out of reach to many patients due to cost and inaccessibility. There is a need for an inexpensive and convenient alternative to professional services. One possible alternative is a medical device that may apply pressure passively, without patient intervention or action after initial device setup, and which may be used at home without the supervision, cost, or aid of a medical professional.

This work is focused on the muscle structures in the posterior neck. Trigger points in the posterior neck region are commonly located in the deep muscle layer (Goubert et al., 2016). The deep layer includes the cervical Multifidus muscles (located between the cervical vertebra), the Suboccipital muscles (located near the first and second cervical vertebra), and the Longus Capitis and Longus Colli muscles, which run parallel to the spine and are critical to the articulation of the vertebrae in the neck. The deep layer is surrounded by several more superficial layers of muscle, including (in order from deep to superficial) the Semispinalis Capitis, the Splenius Capitis, and the Trapezius (Stathakios and Carron, 2023). These muscle structures are surrounded by adipose tissue and skin. Application of physical pressure for the treatment of trigger points in the deep neck muscles must therefore be transmitted through the skin, adipose tissue, and superficial muscle structures before reaching the target location of the treatment.

In this work, experimental data was collected by performing indentation testing on the region of interest of volunteers. Overall tissue displacement as a function of applied static loading was recorded using a novel testing fixture. Next, a two-dimensional axisymmetric finite element (FE) model was constructed to simulate indentation of a soft material with a rigid indenter. The material properties of the elements in the simulation were obtained by minimizing the error between data obtained from experimentation and data obtained through FE simulation. The material properties were iterated and optimized using Bayesian Optimization (BO) methods. The material properties obtained from optimization were then applied to a two-dimensional (2D) plane-strain FE model to approximate a cross-section of the posterior neck. Finally, numerical tests were performed to determine the optimal location and angle of indentation for maximum principal strain in the deep muscle region of the model.

2. Theory and modeling methods

A hypothesis is made that the therapeutic effectiveness of a treatment may be quantified in terms of stresses and strains, such that the results of indentation at different locations and angles can be compared. Since the key therapeutic benefits of the physical pressure application are all mechanically driven by distortion of the tissue, the *maximum principal strain* obtained from the FE analyses is identified as the primary metric for evaluating the therapeutic efficacy at various indentation locations and angles.

Two FE models were developed for this study. The first FE model was an axisymmetric structure which simulated simple indentation for the purpose of optimizing a material model to match the experimental data. The second FE model was a plane-strain model for estimating the maximum principal strain in the deep muscle group in response to pressures at different indentation locations and angles. Both models were constructed with Abaqus/CAE and calculated using the implicit solver.

Indentation testing could be modeled using Hertzian contact mechanics if the material were linearly elastic and experienced small deformations. In the context of trigger-point treatment, the indenter is virtually a rigid body compared to the much softer biological tissues, and the system experiences large deformations. A hyperelasticity model is required to accurately simulate this scenario.

Several hyperelasticity models have been developed and used for modeling the mechanical response of skin and muscle tissues (Singh and Chanda, 2021; Ma et al., 2020; Bosboom et al., 2001; Li et al., 2021; Flynn et al., 2010; Takaza et al., 2013; Payne et al., 2014; Kalra et al., 2016). One of the most commonly used models is the Ogden hyperelastic model (Ogden, 1972), which is a constitutive equation relating the strain energy in a solid to the principal stretch ratios, given in Eq. (1), below.

$$W = \sum_{i=1}^{n} \frac{2\mu}{\alpha_i^2}\left(\lambda_1^{\alpha_i} + \lambda_2^{\alpha_i} + \lambda_3^{\alpha_i} - 3\right) + K(J - 1 - \ln(J)) \tag{1}$$

where W is the strain energy, n is the order of the model, λ_i are the principal stretch ratios, μ is the initial shear modulus, α is the deviatoric exponent, K is a Lagrange multiplier, and J is the bulk modulus. Because this work is concerned with a steady-state pressure application, the effect of viscoelasticity was ignored. The various tissues in the posterior neck were assumed to be incompressible. These assumptions allow for Eq. (1) to be simplified into the "simplified first-order" Ogden model form, shown in Eq. (2):

$$W = \frac{2\mu}{\alpha^2}\left(\lambda_1^{\alpha} + \lambda_2^{\alpha} + \lambda_3^{\alpha} - 3\right) \tag{2}$$

In order to use the simplified first-order Ogden model, it was also assumed that the tissue behaved as a single homogenized isotropic solid. As previously discussed, the tissue structures that make up the posterior neck are comprised of many layers of muscle with differing fiber directions, adipose tissue, connective tissue, and skin. However, if experimental data are gathered from *in vivo* test subjects, the ability to isolate specific tissues for independent testing is restricted. Instead, the Ogden model created in this work is considered to be an *equivalent* homogeneous isotropic material to the collection of the heterogeneous anisotropic tissues in the posterior neck. The equivalent Ogden material (optimized using experimental data) should have displacement-force behavior equivalent to the heterogeneous anisotropic tissues in the posterior neck.

The axisymmetric FE model was generated as a tool for determining the optimal parameters, α^* and μ^*, of the first-order Ogden hyperelastic solid in Eq. (2) (Note: the "*" notation denotes the "optimized" value of the parameter, e.g., α^* is the optimized value of the parameter α). The process for determining α^* and μ^* required a quantification of the error between the experimental data and data generated from the axisymmetric FE model. In experimental testing, tissue displacement was recorded as a function of applied static loading conditions, giving the experimental relationship $\delta_{exp} = f(F_{exp})$, where δ_{exp} is the measured displacement of the tissue and F_{exp} is the static load applied causing each displacement. For the FE simulations, the axisymmetric model was statically loaded in increasing force increments, and the simulated displacement was recorded for each load increment, resulting in an analogous relationship $\delta_{FEM} = f(F_{FEM})$, where δ_{FEM} is the simulated displacement, and F_{FEM} is the corresponding load. The error, e, was quantified as the sum of squared errors (described by Eq. (3)) and was used as the objective function of the minimization using the Simulia Isight software package.

$$e = \int \left[\delta_{FEM}(F) - \delta_{exp}(F)\right]^2 dF \tag{3}$$

Bounds for the design variables, α and μ, were determined by reviewing prior studies on similar testing situations (Ma et al., 2020; Bosboom et al., 2001; Li et al., 2021), as $11 \leq \alpha \leq 20$ and $2\,\text{kPa} \leq \mu \leq 10\text{kPa}$. The Design-of-Experiments (DOE) method was used to create an initial dataset, selecting 16 combinations of starting parameters, α_i and μ_i, using the Optimal Latin Hypercube Sampling (OLHS) technique, and the displacement at each force increment was computed using the axisymmetric FE model. The displacement-force data collected from the FE model was compared to the experimental test results, and the error was calculated using Eq. (3). Once the error corresponding to each of the OLHS-selected material parameter combinations was calculated, the design variable combinations and corresponding errors were collected into a matrix, which was in turn used to generate a continuous error function using Gaussian Process modeling (Bostanabad et al., 2018). After constructing the initial matrix and continuous error function, a Bayesian optimization routine was performed to determine the optimal material property parameters, α^* and μ^*, which resulted in minimized error between experimental and FE-simulated displacement-force data. The optimized material parameters, α^* and μ^*, were then used in the plane-strain FE model to determine the optimal location and angle of indentation for the maximum therapeutic effect.

3. Indentation experiment

Although prior studies have characterized the hyperelastic behavior of skeletal muscle using methodologies similar to those presented in this work, the results obtained in those studies were not directly applicable to this work because they were performed on *in vitro* tissue sample sections (Ma et al., 2020) or on *in vivo* tissues of anesthetized rats (Bosboom et al., 2001). This work is primarily concerned with the mechanical behaviors of *in vivo* human tissue structures in the posterior neck for the treatment of trigger points. As such, experimental data was collected from human volunteers using a novel minimally invasive indentation loading fixture and testing apparatus. Fig. 1 shows an annotated image of the indentation loading fixture.

The loading fixture consists of a 4 mm diameter indenting tip fastened to a weight tray, held in place by a frame with a set of parallel bushings. The indenter tip and weight tray can slide freely along a fixed linear track. A shaft collar is attached to the body of the indenter to allow the position of the weight tray to be locked in place. The frame also contains a sliding dial on one side, which can be locked in place with a thumbscrew. Two adjustable mounting hooks are affixed to the top of the frame to position the loading fixture. The fixture pictured in Fig. 2 is suspended from a ring stand, which is rigidly affixed to a laboratory bench.

Several prior works have used custom-built indentation fixtures to gather mechanical properties from biological tissues. One study used an indentation device to study the material properties of injured brain tissue in mice after presenting injury using a controlled cortical impact device (Chen et al., 2020). The indentation device used in this study consisted of rigid indenter affixed to a motor-controlled frame and used a laser reflection system to measure displacement in response to force. Another similar study also used a custom indentation device for measuring force-displacement data on mouse brain tissue; the device used in this study consisted of a rigid indenter and load cell driven by a linear actuator and used a similar laser sensor for displacement measurement (Qiu et al., 2020). One study used a custom apparatus for micro-indentation of mouse brain tissue at high rates and localized length scales using a piezo actuator stage to indent tissue into a static indenter at controlled constant velocities (MacManus et al., 2018).

While the indentation devices presented in previous works are designed to record data using motor-driven and computer-controlled systems, prior studies have focused on testing the mechanical properties of *in vitro* test specimens of non-human animals (Ma et al., 2020; Bosboom et al., 2001; Chen et al., 2020; Qiu et al., 2020; MacManus et al., 2018). One of the goals of the current study was to collect *in vivo* experimental data from human subjects. The safety of the volunteers was the top priority during experimentation, and as such, the

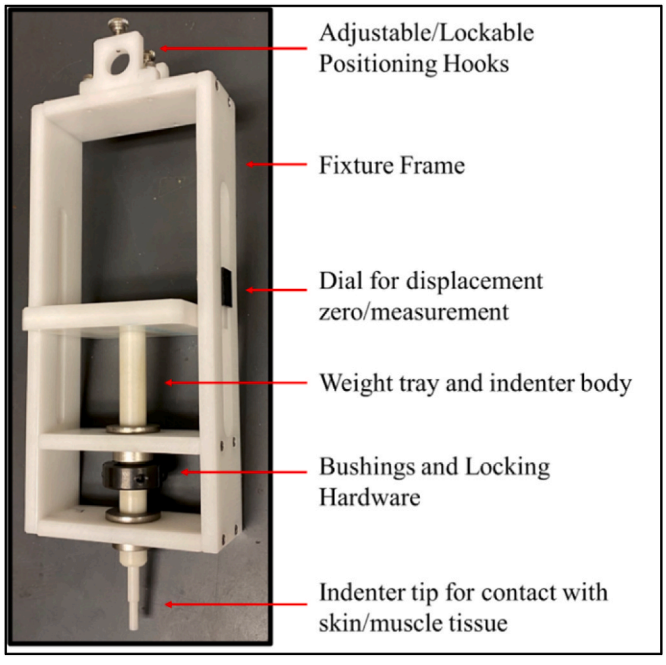

Fig. 1. Novel minimally invasive indentation loading fixture.

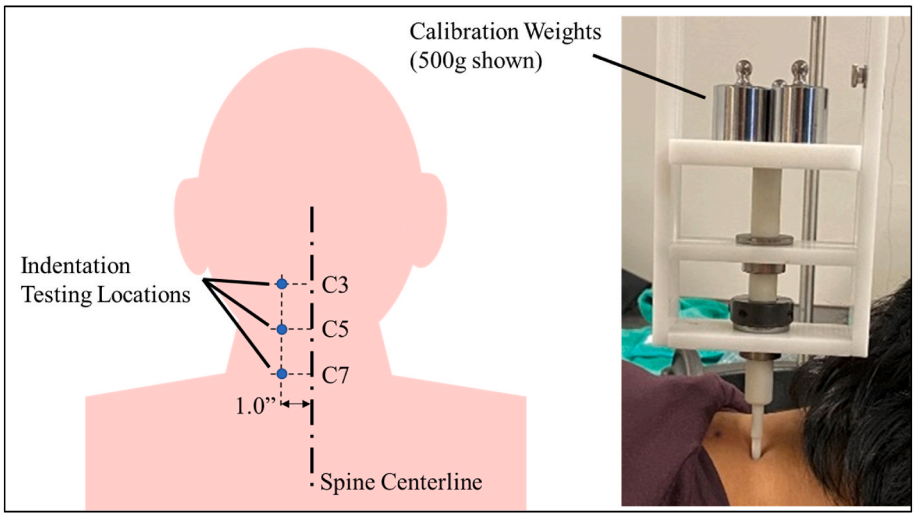

Fig. 2. Indentation locations (left, only one side is shown) and indentation testing (right, only the dominant side was tested).

experiment and fixturing were designed to minimize the risk of harm to the volunteer participating in testing. As such, the fixture was designed to be as minimally invasive to the volunteer as possible. It was also designed to be operated manually by a tester, so that in any event of patient discomfort, the weight of the indenter could be immediately removed and the participant removed from harm. While it would be theoretically possible to design an automated indentation apparatus for human testing, similar to those presented in prior studies on *in vitro* samples (Ma et al., 2020; Bosboom et al., 2001; Chen et al., 2020; Qiu et al., 2020; MacManus et al., 2018), the process of validating the safety for use on humans would be difficult given the scope of this work.

During a typical test, a volunteer was asked to lay in a prone position on the massage table with their hands at their sides. A face cradle was used to support the volunteer's head and neck in a relaxed neutral position. The volunteer was allowed to relax for several minutes to ensure that the transient muscle tightness from getting into testing position had subsided. Once the volunteer was fully relaxed, the indentation testing fixture was positioned over the posterior neck on the volunteer's dominant side, suspended by a laboratory ring stand fixed to a lab bench adjacent to the massage table. The indentation fixture was fixed in place over the volunteer by tightening the adjustable thumbscrews on the positioning hooks (located at the top of the fixture, see Fig. 1) on a fixed horizontal arm of the adjacent ring stand. Indentation testing was performed in three locations approximately 1″ lateral to the sagittal plane on the dominant side, adjacent to the spinous process of cervical vertebrae C3, C5, and C7, as shown in the schematic in Fig. 2. At each location, the indenter was locked in place and positioned directly above the contact point. Once the dial was zeroed, the tray was released, and the weight of the tray was allowed to indent the tissue in the posterior neck at the specified location. After waiting several seconds to allow for viscoelastic effects to subside, calipers were used to measure the displacement of the weight tray by comparing the position of the released weight tray to the zero position, indicated by the locked dial. Once a measurement was taken, the process was repeated, each time adding additional 250 g calibration weights, up to a final weight of 1 kg, plus the weight of the indenter and weight tray. This process was repeated for each of the three testing locations. The picture to the right in Fig. 2 shows a volunteer undergoing indentation testing.

A total of 14 participants volunteered for indentation testing. If volunteers became uncomfortable or began to experience pain during the testing, the weights were removed immediately and testing was terminated. Volunteers were also asked to indicate when their personal pain/discomfort threshold was reached. If testing became painful at a weight lower than 1 kg, the routine was halted at the highest weight recorded, and testing at other locations was only performed up to the volunteer's acceptable threshold.

In total, all volunteers indicated that the highest tested weight (1 kg, plus the weight of the indenter and tray) was the maximum acceptable load; these volunteers contributed 18 displacement-force datapoints each. In total, 252 displacement-force data points were collected. Variation in the data may be explained by various factors that are difficult to quantify, such as muscle tension in the resting state, typical patient posture, skin thickness, and quantity of adipose tissue in the posterior neck. There was no significant difference in displacement-force data between male and female participants. For these reasons, the data was processed into an experimental displacement-force curve by selecting the median displacement recorded for each static load, shown in Fig. 3. Error bars represent ±1 standard deviation.

Because the data was collected by indenting *in vivo* tissues by physically contacting the posterior neck, the experimental median displacement curve shown in Fig. 3 represents the mechanical response of the composite of skin, adipose tissue, muscle structures, and connective tissue between the indenter and (rigid) bone. The Ogden hyperelastic material, optimized by comparing the FE model results to this experimental dataset, is assumed to be an isotropic homogeneous material, as discussed in Section 2. The simulated Ogden material represents a "homogenized equivalent" material to the composite structure measured experimentally. In other words, the optimized Ogden material model may be interpreted as how the tissues of the posterior neck *would*

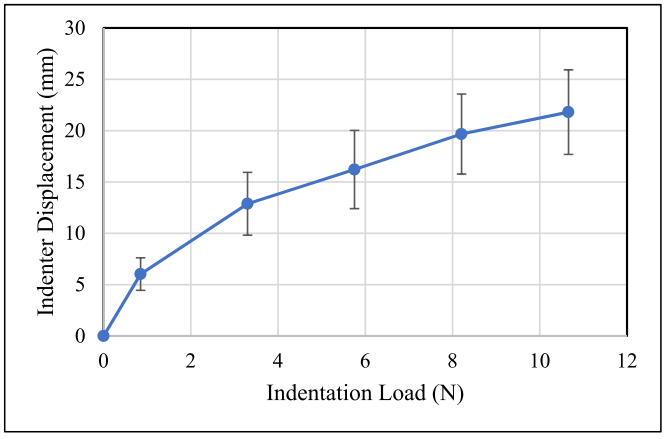

Fig. 3. Experimental median displacement vs. force for data collected from all volunteers.

behave if they were a single homogeneous isotropic material. This assumption is a necessary caveat of performing minimally invasive *in vivo* human tissue testing.

4. Results and discussion

4.1. Ogden model parameters

The DOE stage of the optimization routine selected 16 combinations of α and μ parameters using the OLHS technique. Table 1 summarizes the optimized material parameters for the Ogden material, the minimized error of the model, the number of iterations, and the total time of calculation. The constitutive strain energy equation of the optimized Ogden material is expressed in Eq. (4). Fig. 4 shows a plot of the displacement-force curve of the optimized material model overlayed with the median testing data. Fig. 5 shows the GP model of the predicted error after the optimization process was completed.

4.2. Plane-strain neck section indentation FE modeling

The optimized Ogden material model (Eq. (4)) was implemented in the second FE model, constructed to simulate a cross-section of the posterior neck as a simplified plane-strain model, as discussed in Section 2. The geometry of the neck cross-section was obtained from a prior study that measured the size of the deep neck muscle group across a range of volunteers using an ultrasonography technique (Rankin et al., 2005). An MRI cross-section at the C3 vertebrae (Conley et al., 1997) was imported to a sketch in a CAD model, where the cross-sections of the deep muscle group, outer tissue group, and vertebrae were traced. Sharp corners and complicated geometry were smoothed and simplified to ensure uniformity of the FE mesh. The traced tissue and bone groups were scaled to their average sizes, as reported by (Rankin et al., 2005).

The 4 mm diameter indenter and bone were treated as rigid bodies and were modeled with rigid-body wire elements. The deep muscle group and the outer tissue group were both modeled using rectangular solid deformable elements. Both tissue groups were given the optimized Ogden material properties, and the groups were bonded together at their mutual interface. The thickness of the plane-strain model was 4 mm. Fig. 6 shows the meshed plane-strain FE model, where the average mesh element side length is 1 mm, with the indenter at an angle normal to the skin surface and a location 10° clockwise from the sagittal plane, measured from the centerline of the spine. In Fig. 6, the vertebrae component was fixed in all degrees of freedom.

During simulation, the indenter was only allowed to translate along its central axis. The vertical edge on the left side of the outer tissue component was allowed to translate vertically, but not horizontally, and was fixed in rotation. The horizontal edge on the bottom right side of the outer tissue component was allowed to translate horizontally but not vertically, and it was also fixed in rotation. The elements were otherwise unconstrained. As previously mentioned, the deep muscle component and the outer tissue component were bonded in non-penetration contact with both the bone and indenter rigid bodies. Transverse motion had an associated penalty factor of 0.5. The indenter was loaded to 2.5 N/mm (corresponding to a total load of 10 N for a 4 mm line contact for 1 mm plane-strain elements), after which the maximum principal strain at each node in the deep muscle group was recorded. Fig. 7 shows an example of the deformed neck cross-section at a load of 2.5 N/mm.

Table 1
Ogden model optimization results.

$$W = \frac{2(5.16\ kPa)}{11.9^2}\left(\lambda_1^{11.9} + \lambda_2^{11.9} + \lambda_3^{11.9} - 3\right) \quad (4)$$

Total No. of Iterations	μ* (kPa)	α*	Error (N*mm)^2	Total Time of Calculation
29	5.16	11.90	3.58	51 m 39s

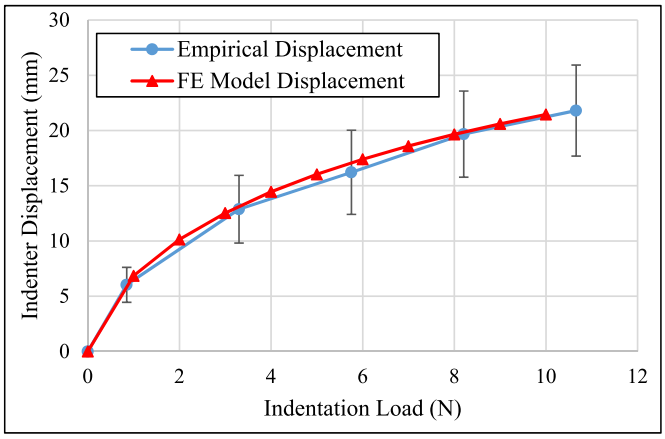

Fig. 4. Comparison of the results from the Optimized FE Model and Mean Experimental Displacement vs. Force.

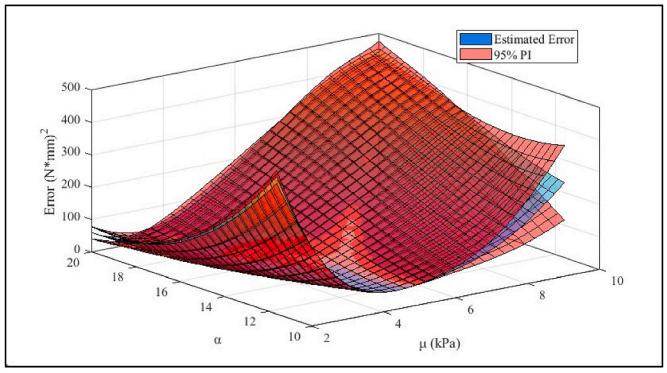

Fig. 5. Gaussian Process (GP) error function and 95% Prediction Interval (PI) for the optimized GP Model.

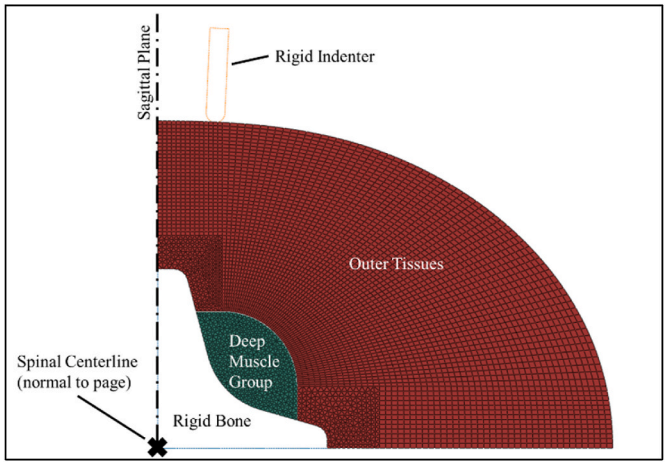

Fig. 6. Plane-Strain FE mesh of the neck cross-sectiontheneck crosssection.

4.3. Optimal indentation location and angle

FE simulations were performed at a range of indenter locations and angles to determine the optimal spatial orientation of the indenter. The optimal spatial orientation is defined as the location and angle of the

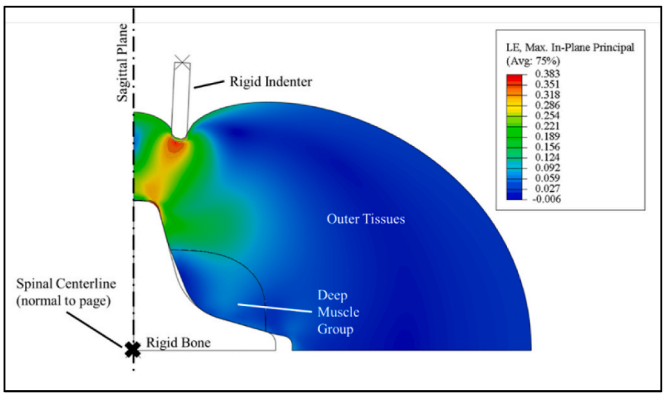

Fig. 7. Deformed neck cross-section indented under a 2.5 N/mm load.

indenter that maximizes the average of the maximum principal strain across all nodes in the deep muscle group. First, the optimal location was determined by testing indentation normal to the surface of the skin at a coarse range of locations. From these simulations, an optimal region was defined, which was then divided into finer increments to determine the precise optimal location of the indenter. A similar technique was used to find the optimal indentation angle at the selected optimal location. The final result is referred to as the optimal indenter spatial orientation (encompassing location and angle).

For each indentation simulation, the maximum principal strain was recorded at each node in the deep muscle group. To quantify the overall effect on the deep muscle group, the "average maximum principal strain" was computed by calculating the arithmetic mean of all nodal values of the maximum principal strain. The average maximum principal strain is the primary metric used to evaluate the strain in the deep muscle group resulting from indentation across the range of simulated indentation locations and angles.

Fig. 8 (a) shows the coarse range of indentation locations. Construction lines from the spinal centerline to the surface of the outer tissue component were drawn every 10°, beginning from the sagittal plane and spanning a range from 10° to 80°. Fig. 8 (b) plots the maximum, minimum and average nodal values of the maximum principal strain in the deep muscle group as a function of indenter location. The initial results suggest that the optimal location is between 20° and 40° from the sagittal plane, measured from the spinal centerline. Fine tuning of the indenter location was performed across the 20°–40° range in increments of 2°, as depicted in Fig. 9 (a). Fig. 9 (b) plots the maximum, minimum, and average nodal values of the maximum principal strain in the deep muscle group as a function of indenter location in the finer range.

The peaks in Fig. 9 (b) are highlighted with enlarged diamond-shaped markers. It was determined that the optimal indenter location was 28° away from the sagittal plane. At this optimal location, indentation simulations were again performed across a coarse range of angles, ranging from −30° to 30° with respect to the normal vector of the outer tissue surface, as shown in Fig. 10 (a). Simulations across this coarse range were spaced in 10° increments. Fig. 10 (b) plots the maximum, minimum and average nodal values of the maximum principal strain in the deep muscle group as a function of indenter angle across the coarse range. Note that negative and positive angle values refer to angles measured clockwise and counterclockwise from the normal vector, respectively.

Based on the results from simulations in the coarse angle range, the maximum of the average maximum principal strains appeared to be somewhere in the range of 0–20° (counterclockwise) from the normal vector at the optimal location. Simulations were repeated across indentation angles in this range in increments of 4°, as depicted in Fig. 11 (a). The results of the maximum, minimum, and average nodal values of the maximum principal strain in the deep muscle group are plotted in Fig. 11 (b) as a function of indentation angle in the finer range.

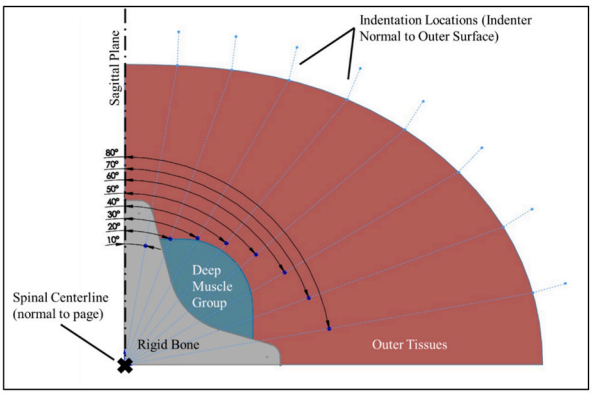

(a)

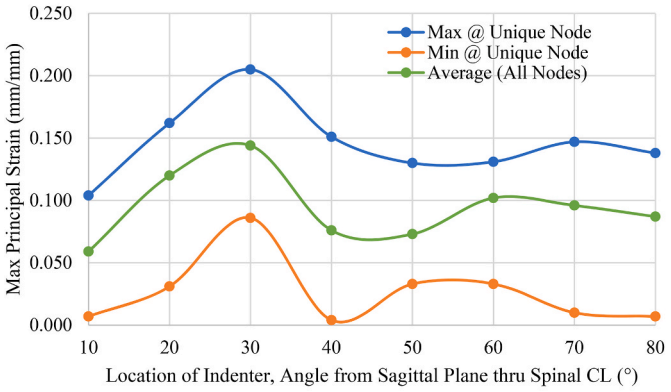

(b)

Fig. 8. Coarse-range indenter location simulation results. (a) Model setup showing the indentation locations simulated in the coarse location range; (b) Maximum, minimum and average nodal values of maximum principal strain in the deep muscle group vs. indenter location, coarse location range. The "unique node" refers to a specific nodal point within the deep muscle group.

The peaks in Fig. 11 are highlighted with enlarged diamond-shaped markers, which determined that the optimal indentation angle should be 8° counterclockwise from the average of the maximum principal strains in the deep muscle group. Thus, the final optimized spatial orientation of the indenter should be at a location 28° lateral from the sagittal plane measured from the spinal center axis, with an indentation angle of 8° counterclockwise from the normal vector of the outer tissue surface at this location.

The optimal location and angle of indentation from the previous section were used to simulate the overall strain field. Fig. 12 (a) shows the deformed skin material, and Fig. 12 (b) maps the maximum principal strain in the deep muscle group in this configuration.

The deep muscle group mesh consisted of 420 nodes, and the maximum principal strain value was recorded for each node, giving a quantitative approximation for the amount of physical deformation (stretching) that took place at each point in this muscle group. The data reported in Fig. 9 (b), **10 (b)**, **11 (b)**, and **12 (b)** provide the recorded maximum and minimum individual values in the dataset, as well as the average of all values across the entire deep muscle group. The coarse-range location simulation result (Fig. 9 (b)) suggests initially that the maximum, minimum, and average of the maximum principal strains all occurred around the same location. Upon further inspection in the fine-range location simulations (Fig. 10 (b)), it was noted that the minimum and average strain values both occurred at the location of 28° from the sagittal plane, while the maximum strain value was recorded at 32° from the sagittal plane. The minimum, maximum, and average values of

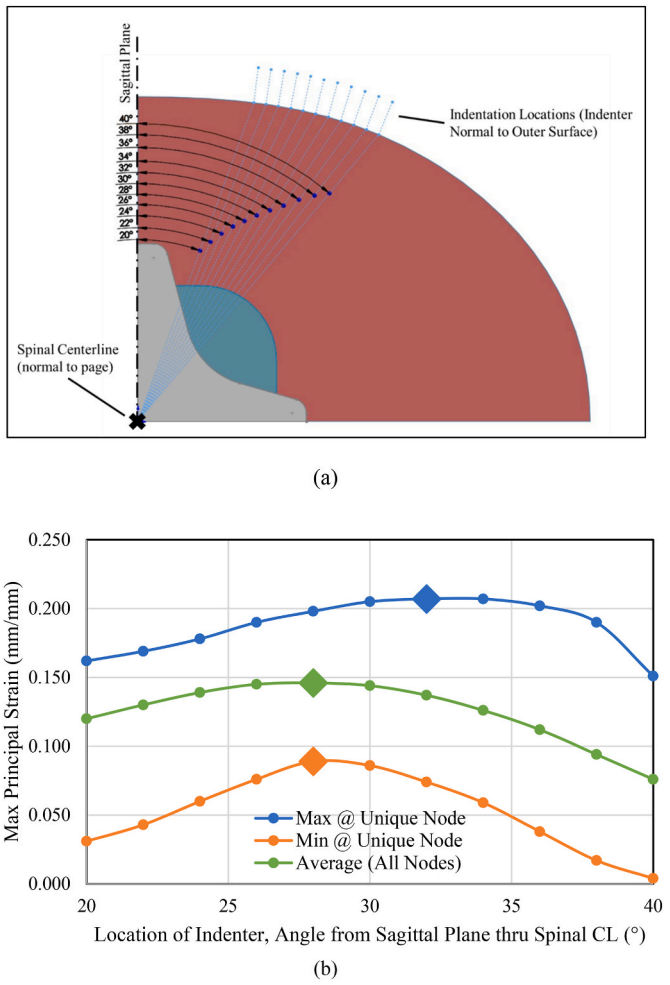

Fig. 9. Fine-range indenter location simulation results. (a) Model setup showing the indentation locations simulated in the fine location range; (b) Maximum, minimum and average nodal values of maximum principal strain in the deep muscle group vs. indenter location, fine location range. The maximum values are highlighted with diamond markers. The "unique node" refers to a specific nodal point within the deep muscle group.

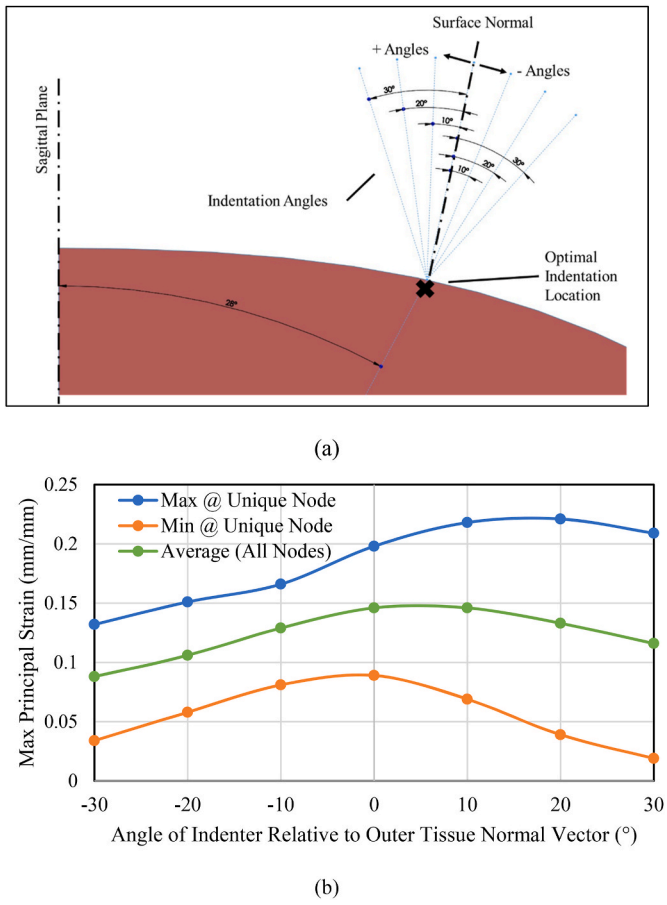

Fig. 10. Coarse-range indentation angle simulation results. (a) Model setup showing the indentation locations simulated in the coarse angle range; (b) Maximum, minimum and average nodal values of maximum principal strain vs. indentation angle in the coarse range. The "unique node" refers to a specific nodal point within the deep muscle group.

maximum principal strain continued to diverge as the angle of the indenter was modulated at the optimal location. Fig. 12 (b) reveals that the peak value of the minimum of the maximum principal strain occurs when the indenter was normal to the outer tissue surface, and that of the average maximum principal strain occurred at 8° counterclockwise, while that of the maximum of the maximum principal strain occurred at 16° counterclockwise. The optimized spatial orientation of indentation identified as a result of this simulation is dependent on the shape of the deep muscle group. The deep muscle group size and shape were modeled based on data from a range of volunteers using an ultrasonography technique (Rankin et al., 2005).

The divergence of the peak values of the unique nodal strains from the peak value of the average of the maximum principal strain as the angle of the indenter was increased suggests the formation of stress concentrations in specific areas of the deep muscle group, or non-uniform strain distributions. The optimal indentation location and angle was identified by selecting the configuration at which the average of the maximum principal strain across all of the nodes in the deep muscle group reached a peak, as opposed to selecting the location and angle corresponding to the maximum of a unique nodal strain, to avoid favoring indentation orientations which cause stress concentrations over orientations where the entire muscle group is deformed more evenly.

It should be noted that the model presented has several limitations. Firstly, a three-dimensional FE model would likely provide more accurate simulation results, although the computation cost would be greatly increased. Secondly, the population that participated in indentation experiments consisted mainly of healthy individuals between 22 and 30 years of age; this population is demographically narrow and may not fully represent populations more vulnerable to neck problems, such as older persons. Thirdly, it is difficult to quantify the absolute therapeutic effect of indentation. In the optimized configuration, the nodal average strain was 0.148 mm/mm. While this is the best observed result within the context of the simulation, there currently exists no mechanism by which the actual therapeutic benefit can be directly quantified by elongating the deep neck muscles by an average of 14.8%; clinical studies are necessary to quantify any therapeutic benefits. Finally, the physical size and locations of muscles may vary greatly between individuals; for example, a young male with a high body-mass index (BMI) may have a much larger neck circumference than an elderly female with a low BMI. The optimal location and angle of indentation may vary depending on how greatly a particular person's physical size differs from the average. Additionally, the optimized spatial orientation of indentation is dependent on the shape and size of the "average" deep muscle group as constructed for the FE model; however, individuals with slightly differently shaped deep muscle groups may still experience similar optimal indentation at orientations to the optimized result presented in this work due to the nature of strain average.

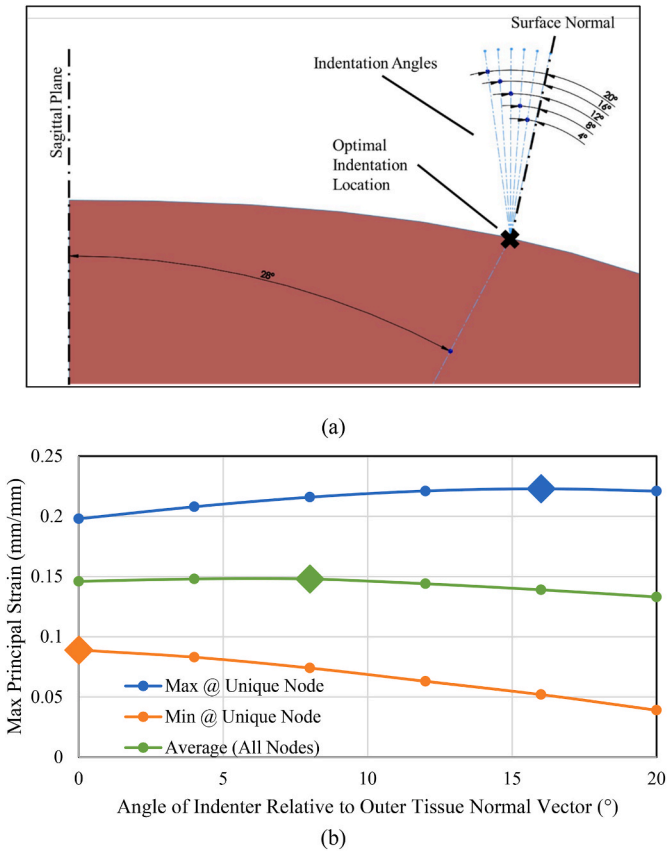

Fig. 11. Fine-range indentation angle simulation results. (a) Model setup showing the indentation locations simulated in the fine angle range; (b) Maximum, minimum and average nodal values of maximum principal strain vs. indentation angle in the fine angle range. The maximum values are highlighted with diamond markers. The "unique node" refers to a specific nodal point within the deep muscle group.

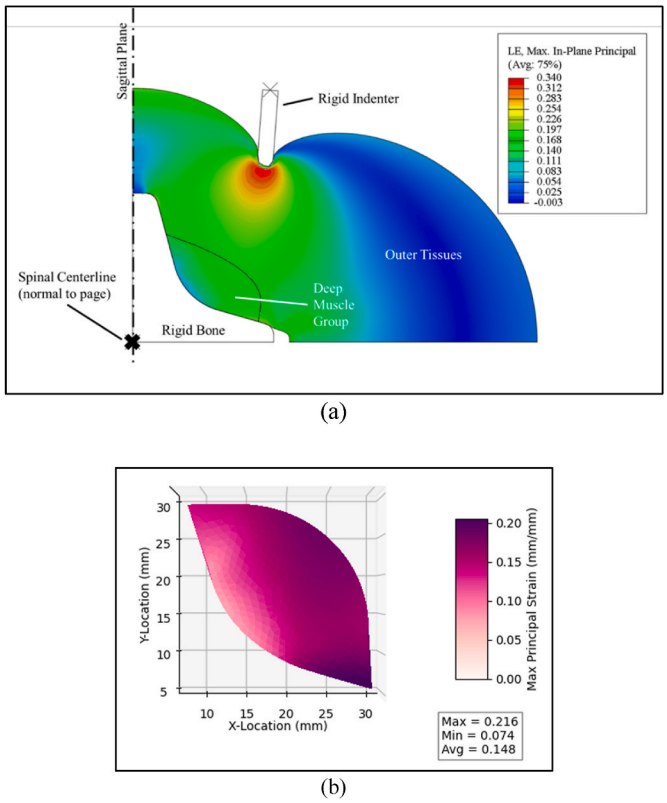

Fig. 12. Behavior of the neck muscle under the indentation at the optimal indentation location and angle. (a) Overall deformation; (b) Maximum principal strain in the deep muscle group (displayed in the "undeformed" state for visual clarity).

5. Conclusion

Trigger points are a common source of myofascial pain and reduced range of motion. There is a need for medical devices for passive at-home trigger point treatment, and the development of such devices requires a methodology for obtaining feasible design schemes from the mechanical response of *in vivo* biological tissues. This work primarily yielded a framework for the mechanics of trigger point treatment design, consisting of experimentally supported biological tissue material modeling, treatment simulation, and determination of the optimal device design parameters to achieve the desired mechanical effects in the tissue structure of interest.

The tissue of the posterior neck was the focus of this work. The experimental data were collected on the displacement of the composite tissues in the posterior neck in response to steady-state fixed load indentation, involving a total of 14 healthy volunteers between 22 and 30 years of age. A material model was developed, using the first-order Ogden hyperelastic constitutive equation, and optimized to mimic the load-displacement behavior observed from the indentation experiments. The optimized material model was used to construct a plane-strain FE model of a cross-section of the posterior neck. Indentation at a constant load was performed at a range of locations and angles along the surface of the simulated neck tissue. Treatment design was informed by modulating the location and angle of indentation treatment to find the peak average value of the maximum principal strain local to the deep muscle group in the posterior neck. Conclusions from this work are as follows.

1. The curve of the median displacement-force experimental data resembled that of a first-order Ogden hyperelastic material. The optimized Ogden model has an initial shear modulus (μ) of 5.16 kPa and a deviatoric exponent (α) of 11.90, with a minimized sum of squared errors of 3.58 $(N*mm)^2$.
2. The effectiveness of treatment was quantified by maximizing the average of the maximum principal strain induced by indentation across all nodes in the deep muscle group of the neck tissue FE model. The optimal location of indentation was found to be 28° lateral from the sagittal plane, measured along the surface of the posterior neck about the spinal centerline. The optimal angle of the indenter at this location was found to be 8° counterclockwise from the neck tissue surface normal vector (at the optimal location).
3. Increasing the angle of indentation beyond the optimal angle tended to increase the peak unique nodal value of the maximum principal strain but decrease the average of the maximum principal strain in the deep muscle group, suggesting that more extreme indentation angles may result in stress concentrations and non-uniformity within the deep muscle group.

CRediT authorship contribution statement

Conor Shanley: Writing – review & editing, Writing – original draft, Validation, Methodology, Investigation, Formal analysis, Data curation, Conceptualization. **Q. Jane Wang:** Writing – review & editing, Project administration, Methodology, Investigation, Formal analysis, Conceptualization. **Bruce Livingston:** Writing – review & editing, Methodology, Conceptualization.

Declaration of competing interest

The authors declare that they have no known competing financial interests or personal relationships that could have appeared to influence the work reported in this paper.

Data availability

Data will be made available on request.

Acknowledgements

The authors would like to thank Professor Yonggang Huang and Wei Chen at Northwestern University, United States, for valuable suggestions and assistance. Support was also provided by graduate students Xiaoman Wang, Tobias Martin, Nicole Dorcy, Jannat Ahmed, Henry Soewardiman, and Yigitcan Comlek (Northwestern University). Medical background information and expertise were enhanced by Karlie Bless, PT, DPT, and Eric Hauser, MD. Contributions by the volunteers for indentation testing are also gratefully acknowledged.

List of Abbreviations

MPS	Myofascial Pain Syndrome
FDM	Fascial Distortion Model
CNS	Central Nervous System
FE	Finite Element
BO	Bayesian Optimization
DOE	Design of Experiments
GP	Gaussian Process
OLHS	Optimal Latin Hypercube Sampling
PI	Prediction Interval
BMI	Body Mass Index
SCF	Spatial Correlation Function
CDF	Cumulative Distribution Function
PDF	Probability Density Function

Appendix. Bayesian Optimization & Gaussian Process Modeling

In this work, the Gaussian process (GP) regression was performed using the ordinary Kriging method (Williams, 1998). GP regression is a method of spatial interpolation used for predicting the values of non-measured datapoints using a weighted average of the surrounding datapoints, while also providing a quantification of the uncertainty associated with predicted datapoints. Eq. (A1) expresses a general form of the GP regression model.

$$\widehat{y}(\boldsymbol{x}) = \sum_{i=1}^{n} \beta_i f_i(\boldsymbol{x}) + z(\boldsymbol{x}) \tag{A1}$$

This equation may also be expressed more concisely in matrix form, shown in Eq. (A2),

$$\widehat{y}(\boldsymbol{x}) = \boldsymbol{\beta}^{\boldsymbol{T}} \boldsymbol{f}(\boldsymbol{x}) + z(\boldsymbol{x}) \tag{A2}$$

where $\widehat{y}$ is the predicted value of the regression model based on the input data $\boldsymbol{x}$, which is expressed as a matrix because the input data may be multi-dimensional. The first term on the right-hand side of the equation, $\boldsymbol{\beta}^{\boldsymbol{T}} \boldsymbol{f}(\boldsymbol{x})$, is the prediction model, which captures the global trend of the data, similar to standard linear and polynomial regression methods. The second term on the right-hand side of the equation, $z(\boldsymbol{x})$, is the departure model, which captures the uncertainty of the prediction model. The departure model is a stochastic function characterized by a Gaussian distribution with a zero mean. The covariance between each pair of input points $\boldsymbol{x}^i, \boldsymbol{x}^j$ is defined by a spatial correlation function (SCF), per Eq. (A3).

$$Cov\left(\boldsymbol{x}^i, \boldsymbol{x}^j\right) = \sigma^2 R\left(\boldsymbol{x}^i, \boldsymbol{x}^j\right) \tag{A3}$$

where σ^2 is the variance of the stochastic departure model $z(\boldsymbol{x})$, and $R(\boldsymbol{x}^i, \boldsymbol{x}^j)$ is the SCF of the dataset $\boldsymbol{x}$. Note that in the presented notation, the superscripts i and j denote the "i^{th}" and "j^{th}" elements in the data matrix $\boldsymbol{x}$, and should not be confused as exponents. In this work, the Gaussian SCF was used, as described in Eq. (A4).

$$R\left(\boldsymbol{x}^i, \boldsymbol{x}^j\right) = \exp\left[-\sum_{k=1}^{m} \theta_k \left(\boldsymbol{x}_k^i - \boldsymbol{x}_k^j\right)^2 \right] \tag{A4}$$

where the spatial correlation function is driven by the correlation parameter θ_k, and $k = 1, \ldots m$ is the number of dimensions in the dataset. The covariance between any two input data points is equal to the variance of the stochastic departure model $z(\boldsymbol{x})$ multiplied by the SCF. The SCF is an exponential function of the squared difference between each of the points in the input dataset, weighted by the correlation parameter θ_k. In general, the larger the correlation parameter for two input datapoints, the smaller the correlation between those points. The parameters of the GP regression model $\boldsymbol{\beta}, \sigma^2, \boldsymbol{\theta}$ may be determined using a variety of optimization techniques; in this work, the Maximum Likelihood Estimation was used (Bostanabad et al., 2018).

In this work, sample data used as inputs to the GP regression model consisted of two inputs, the Ogden material parameters μ and α, and the corresponding error e. The data is expressed in matrix form as $\boldsymbol{D} = \left[\vec{\mu} \quad \vec{\alpha} \quad \vec{e} \right]$. The GP regression model for this dataset is expressed in terms of these variables in Eq. (A5).

$$\widehat{e}_{GP}(\mu,\alpha) = \beta\widehat{f}(\mu,\alpha) + \widehat{z}(\mu,\alpha) \tag{A5}$$

The first term on the right-hand side of equation (A5) corresponds to the GP regression mean function, and the second term on the right-hand side of the equation corresponds to the stochastic departure model. Given a limited selection of initial input data $\boldsymbol{D}$, the utility function may be expressed per Eq. (A6).

$$I(\mu,\alpha) = \max[0, (\min(\overrightarrow{e}) - \widehat{e}_{GP}(\mu,\alpha))] \tag{A6}$$

Since the data used to construct the GP regression model does not encompass the entirety of the input space, the expected improvement in the error at a given combination of input parameters is given by the expected value of the utility function, expressed in Eq. (A7).

$$E[I(\mu,\alpha)] = (\min(\overrightarrow{e}) - \beta\widehat{f}(\mu,\alpha))\Phi\left(\frac{\min(\overrightarrow{e}) - \beta\widehat{f}(\mu,\alpha)}{\widehat{z}(\mu,\alpha)}\right) + \widehat{z}(\mu,\alpha)\varphi\left(\frac{\min(\overrightarrow{e}) - \beta\widehat{f}(\mu,\alpha)}{\widehat{z}(\mu,\alpha)}\right) \tag{A7}$$

In Eq. (A7), the $\Phi(x)$ operator represents the standard normal cumulative distribution function (CDF), and the $\varphi(x)$ operator represents the standard normal probability density function (PDF). The Bayesian optimization acquisition function is then defined as the maximum value of the expected improvement function, per equation (A8).

$$a_{BO}(\mu,\alpha) = \max[E(I(\mu,\alpha))] \tag{A8}$$

The Bayesian optimization process selects the error testing point by computing the expected value of the improvement to the objective function and picking the material parameters corresponding to the maximum expected improvement. The true error is computed with these selected parameters using Abaqus and Data Matching modules in Simulia Isight; if the true error is greater than the error threshold, the optimization loop continues, and the GP regression model is regenerated using the new additional datapoint generated by the prior optimization iteration. If the true error value is below the error threshold, optimization is terminated.

References

Adamczyk, J.G., et al., 2020. Does the type of foam roller influence the recovery rate, thermal response and DOMS prevention? PLoS One 15 (6).

Adams, R., White, B., Beckett, C., 2010. The effects of massage therapy on pain management in the acute care setting. International Journal of Therapeutic Massage & Bodywork 3 (1), 4–11.

Alvarez, D.J., Rockwell, P.G., 2002. Trigger points: diagnosis and management. Am. Fam. Physician 65 (4), 653–660.

Astokorki, A.H.Y., Mauger, A.R., 2017. Transcutaneous electrical nerve stimulation reduces exercise-induced perceived pain and improves endurance exercise performance. Eur. J. Appl. Physiol. 117 (3), 483–492.

Bosboom, E.M.H., et al., 2001. Passive transverse mechanical properties of skeletal muscle under in vivo compression. J. Biomech. 34, 1365–1368.

Bostanabad, R., et al., 2018. Leveraging the nugget parameter for efficient Gaussian process modeling. Int. J. Numer. Methods Eng. 114 (5), 501–516.

Campbell, T.S., Johnson, J.A., Zernicke, K.A., 2020. Gate control theory of pain. Encyclopedia of Behavioral Medicine. Springer Publishing, New York, NY, USA.

Chen, Y., et al., 2020. Measurement of viscoelastic properties of injured mouse brain after controlled cortical impact. Biophysics Reports 6 (4), 137–145.

Conley, M.S., et al., 1997. Specificity of resistance training responses in neck muscle size and strength. Eur. J. Appl. Physiol. 75, 443–448.

Delgado, E.V., Cascos-Romero, J., Esconda, C.G., 2010. Myofascial pain associated to trigger points: a literature review. Part 2: differential diagnosis and treatment. Med. Oral, Patol. Oral Cirugía Bucal 15 (4), 639–643.

Flynn, C., Taberner, A., Nielsen, P., 2010. Mechanical characterization of *in vivo* human skin using a 3D force-sensitive micro-robot and finite element analysis. Biomech. Model. Mechanobiol. 10, 27–38.

Gladden, L.B., 2008. 200th anniversary of lactate research in muscle. Exerc. Sport Sci. Rev. 26 (3), 109–115.

Goubert, D., et al., 2016. Structural changes of lumbar muscles in non-specific low back pain: a systematic review. Pain Physician 19 (7).

Grieve, R., et al., 2011. The immediate effect of soleus trigger point pressure release on restricted ankle joint doriflexion: a pilot randomised controlled trial. J. Bodyw. Mov. Ther. 15 (1), 42–49.

Ickowicz, E., et al., 2009. Pharmacological management of persistent pain in older persons. J. Am. Geriatr. Soc. 57 (8), 1331–1346.

Kalra, A., Lowe, A., Al-Jumaily, A.M., 2016. Mechanical behavior of skin: a review. J. Mater. Sci. Eng. 5 (4).

Levangie, P.K., Norkin, C.C., Lewek, M.D., 2019. Joint Structure & Function A Comprehensive Analysis, sixth ed. F. A. Davis Company, Philadelphia, PA, USA.

Li, F., et al., 2021. A high-fidelity human cervical muscle finite element model for motion and injury studies. Transportation Safety and Environment 3 (4).

Ma, F., et al., 2020. In vitro compressive properties of skeletal muscles and inverse finite element analysis: comparison of human versus animals. J. Biomech. 109.

MacManus, D.B., Murphy, J.G., Gilchrist, M.D., 2018. Mechanical characterisation of brain tissue up to 35% strain at 1, 10, and 100/s using a custom-built micro-indentation apparatus. J. Mech. Behav. Biomed. Mater. 87, 256–266.

Montanez-Aguilera, F.J., et al., 2010. Changes in a patient with neck pain after application of ischemic compression as a trigger point therapy. J. Back Musculoskelet. Rehabil. 23 (2), 101–104.

Mukherjee, A., Chakravarty, A., 2010. Spasticity mechanisms – for the clinician. Front. Neurol. 1 (149).

Niel-Asher, S., 2014. The Concise Book of Trigger Points: A Professional and Self-Help Manual. North Atlantic Books, Berkeley, CA, USA.

Ogden, R.W., 1972. Large deformation isotropic elasticity – on the correlation of theory and experiment for incompressible rubberlike solids. Proceedings of the Royal Society of London: Series A, Mathematical and Physical Sciences 326 (1567), 565–584.

Payne, T., et al., 2014. Development of novel synthetic muscle tissues for sports impact surrogates. J. Mech. Behav. Biomed. Mater. 41, 357–374.

Qiu, S., et al., 2020. Viscoelastic characterization of injured brain tissue after controlled cortical impact (CCI) using a mouse model. J. Neurosci. Methods 330, 108463.

Rankin, G., Stokes, M., Newham, D.J., 2005. Size and shape of the posterior neck muscles measured by ultrasound imaging: normal values in males and females of different ages. Man. Ther. 10, 108–115.

Simons, D.G., Travell, J.G., Simons, L.S., 1999. Myofascial Pain and Dysfunction, the Trigger Point Manual. Williams & Wilkins, Philadelphia, PA, USA.

Singh, G., Chanda, A., 2021. Mechanical properties of whole-body soft human tissues: a review. Biomedical Materials 16.

Stathakios, J., Carron, M.A., 2023. *Anatomy, Head And Neck, Posterior Cervical Region*, Treasure Island. StatPearls Publishing, FL, USA.

Takaza, M., Moerman, K.M., Simms, C.K., 2013. Passive skeletal muscle response to impact loading: experimental testing and inverse modelling. J. Mech. Behav. Biomed. Mater. 27, 214–225.

Wiaderna, K., Selegrat, M., Hadamus, A., 2022. Effect of a single session of facial distortion model manual physiotherapy and a selected foam rolling technique on treatment outcomes in cervical spine overload. Ortop. Traumatol. Rehabil. 22 (2), 131–141.

Williams, C.K.I., 1998. Prediction with Gaussian processes: from linear regression to linear prediction and beyond. Learning in Graphical Models. Kluwer Academic Publishers, Boston, MA, USA, pp. 599–621.

Yap, E.C., 2007. Myofascial pain – an overview. Annals Academy of Medicine 36 (1), 43–48.